



HAL
open science

Acoustic responses of underwater superhydrophobic surfaces subjected to an intense pulse

Adrien Bussonnière, Qingxia Chad Liu, Peichun Amy Tsai

► **To cite this version:**

Adrien Bussonnière, Qingxia Chad Liu, Peichun Amy Tsai. Acoustic responses of underwater superhydrophobic surfaces subjected to an intense pulse. *Journal of Fluid Mechanics*, 2023, 956, pp.A32. 10.1017/jfm.2023.61 . hal-04009685

HAL Id: hal-04009685

<https://hal.science/hal-04009685v1>

Submitted on 1 Mar 2023

HAL is a multi-disciplinary open access archive for the deposit and dissemination of scientific research documents, whether they are published or not. The documents may come from teaching and research institutions in France or abroad, or from public or private research centers.

L'archive ouverte pluridisciplinaire **HAL**, est destinée au dépôt et à la diffusion de documents scientifiques de niveau recherche, publiés ou non, émanant des établissements d'enseignement et de recherche français ou étrangers, des laboratoires publics ou privés.



Distributed under a Creative Commons Attribution - NonCommercial - NoDerivatives 4.0 International License

Banner appropriate to article type will appear here in typeset article

1 **Acoustic responses of underwater superhydrophobic** 2 **surfaces subjected to an intense pulse**

3 **Adrien Bussonnière^{1,2,3}†, Qingxia Chad Liu² and Peichun Amy Tsai³‡**

4 ¹Laboratoire Matière et Systèmes Complexes, Université Paris Cité, UMR CNRS 7057, 75013 Paris,
5 France

6 ²Department of Chemical and Materials Engineering, University of Alberta, Edmonton, AB, T6G 1H9,
7 Canada

8 ³Department of Mechanical Engineering, University of Alberta, Edmonton, AB, T6G 1H9, Canada.

9 (Received xx; revised xx; accepted xx)

10 Underwater stability of an air layer trapped in a micro-structure, plastron, is critical in
11 drag reduction application. Here we investigate the wetting state and plastron stability upon
12 underwater superhydrophobic surfaces (SHS) under an intense acoustic drive. Flat surfaces
13 and SHS are subjected to short acoustic pulses of different intensities. At low amplitude,
14 the comparison between the results of various surfaces shows that plastron behaves like a
15 water-air interface, whose presence can be detected from the phase of the reflected acoustic
16 waves. At moderate intensity, a wetting transition towards a completely wetting state is
17 observed and shown to be triggered by a sufficiently large acoustic radiation pressure. This
18 wetting transition is well captured by a simplified model by balancing radiation pressure
19 with the critical capillary pressure for the interface sliding. Cavitation clouds appear under
20 strong excitation; their sizes and position greatly depend on the surface acoustic boundary
21 condition. For a SHS in a Cassie-Baxter state (with an air layer), cavitation clouds appear
22 at specific locations (from the solid surface) corresponding to the pressure anti-node of the
23 transient standing wave generated by the reflection. This study unprecedentedly demonstrates
24 the capability of acoustic waves to monitor and characterize plastron stability with low and
25 moderate amplitudes, respectively.

26 **Key words:** acoustics, cavitation, contact lines, wetting and wicking

27 **1. Introduction**

28 Superhydrophobic surfaces (SHS) are bio-inspired surfaces composed of hydrophobic
29 patterned micro/nano-structures (Quéré 2008). The combination of roughness and hydropho-
30 bicity makes such surfaces water-repellent, an attracting property for various applications
31 (Quéré 2008). When immersed in water, SH surfaces can trap an air layer, also called
32 plastron, inside the microstructure (Bobji *et al.* 2009), opening the avenue for drag reduction

† Email address for correspondence: adrien.bussonniere@cnrns.fr

‡ Email address for correspondence: peichun.amy.tsai@ualberta.ca

33 applications since such surfaces exhibit significant effective slipping lengths (Rothstein
34 2010). However, the stability of the air layer against pressure fluctuations, induced by
35 potentially turbulent flow (Seo *et al.* 2018; Castagna *et al.* 2018) or against gas dissolution
36 (Poetes *et al.* 2010), is a crucial problem in the development of such SH coatings. Indeed,
37 the air layer can be pushed inside the microstructure, and the superhydrophobic state breaks
38 down (Moulinet & Bartolo 2007; Reyssat *et al.* 2007), i.e., a wetting transition occurs from
39 a (gas-trapping) Cassie-Baxter to a (completely wetting) Wenzel state, and the surface drag
40 coefficient increases dramatically (Karatay *et al.* 2013). Although substantial efforts have
41 been invested in developing robust SHS (Verho *et al.* 2012; Xiang *et al.* 2017), plastron
42 stability still limits the useful applications of SHS.

43 To better understand superhydrophobic breakdown, the wetting transition has been ex-
44 tensively studied in quasi-static configurations, such as in evaporating droplet (McHale
45 *et al.* 2005; Jung & Bhushan 2007; Tsai *et al.* 2010; Bussonnière *et al.* 2017), with
46 surfactant additives (Shardt *et al.* 2019; Aldhaleai & Tsai 2022), under different drop volume
47 (Yoshimitsu *et al.* 2002) and pressure (Lafuma & Quéré 2003), or in dynamic situations, e.g.,
48 drop impact (Bartolo *et al.* 2006) or under surface vibrations (Bormashenko *et al.* 2007).
49 For immersed SHS, wetting transition was mainly studied under static pressure (Poetes *et al.*
50 2010; Lv *et al.* 2014). However, in the main application of underwater SHS (drag reduction),
51 pressure fluctuates due to the flow, which can become turbulent (Seo *et al.* 2018).

52 Acoustic waves have the ability to impose precise pressure over an extensive frequency
53 range. Moreover, sound waves strongly interact with bubbles (e.g., a plastron can be seen
54 as an elongated bubble) in liquid. Therefore, an acoustic method can be a well-suited tool
55 for submerged SHS characterisation. Promising plastron acoustic monitoring was obtained
56 by using longitudinal waves coming from the solid, from beneath the surface, to probe
57 the wetting state by monitoring the back-scattered waves (Saad *et al.* 2012; Dufour *et al.*
58 2013; Li *et al.* 2014). However, this method requires calibration or precise knowledge of the
59 morphology of the SH coating. Furthermore, elastic acoustic waves are not in contact with
60 the air-water interface and, therefore, prohibit direct interaction with the gas-liquid interface.
61 In (Sudeepthi *et al.* 2020), drop wetting transitions were triggered by surface acoustic waves
62 through indirect interaction, i.e., through drop oscillations. Other authors studied submerged
63 SHS as potential acoustic meta-materials (Tong *et al.* 2020; Feng *et al.* 2019). However, the
64 strong interaction between acoustic waves coming from the liquid phase and a SHS remains
65 unexplored. Such an acoustic method is expected to be versatile since the technique uses
66 only one portable transducer to excite and receive waves, similar to non-destructive testing.
67 The acoustic technique would be hence well suited to characterize SHS in applications or
68 in complex environments (e.g., underwater) whereby classical optical techniques, such as
69 confocal microscopy (Papadopoulos *et al.* 2013) or light interference (Moulinet & Bartolo
70 2007) which require a microscope and transparent substrate, cannot be used.

71 In this paper, we propose to fill the gap by exploring experimentally the behavior of
72 immersed superhydrophobic surfaces subjected to short acoustic pulses of varying intensity.
73 Different SHS and flat surfaces are exposed to acoustic pulses using the experimental setup
74 described in 2. At low acoustic amplitude, various surfaces show different acoustic boundary
75 conditions described in Section 3.1. Cavitation behavior is characterized at high amplitude
76 in Section 3.2. The wetting transition is observed at an intermediate intensity and discussed
77 in Section 3.3.

78 2. Experimental setup

79 The experimental setup shown in Figure 1 consists of a High Intensity Focused Ultrasound
80 (HIFU) transducer (Sonic Concepts H101, 1.1 MHz) which focuses short acoustic pulses onto

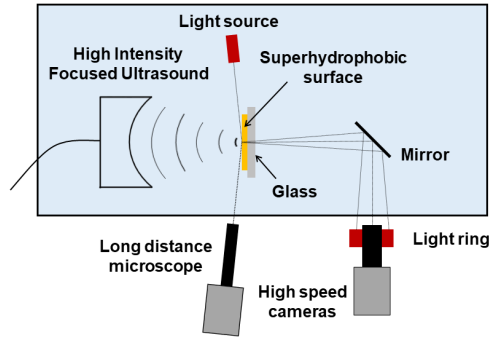


Figure 1: Schematic of the experimental setup. Short acoustic pulses are emitted by a High Intensity Focused Ultrasound transducer and focused upon the tested surface held by a glass coverslip. The dynamic is monitored from the side and from the bottom by two high speed cameras.

81 an immersed surface with a circular focal area of 3 mm in diameter. The acoustic excitation
 82 comprises 3 cycles of 1.1 MHz. To calibrate the pressure, we first map the acoustic field at
 83 a constant low amplitude using a needle hydrophone (Onda HNR-0500, bandwidth 0.25-10
 84 MHz) mounted on 3D axis displacement stage and use the open source code solving nonlinear
 85 propagation (Khokhlov-Zabolotskaya-Kuznetsov equation) developed by Joshua Soneson
 86 (Soneson 2009; Maruvada *et al.* 2015) to fit the experimental results. The hydrophone is then
 87 kept at the focal point (for low amplitude) and at the secondary lobe (for high amplitude), and
 88 the amplitude is varied. Combining the acoustic mapping, pressure amplitude measurements,
 89 and the nonlinear simulation, we finally obtain the calibrated pressure field for a specific
 90 supply voltage of the acoustic drive (see Appendix A).

91 Four surfaces were used in this study to compare different behavior under acoustic excita-
 92 tion: glass, flat PDMS, and two PDMS SH surfaces. The SH and flat PDMS surfaces were
 93 first placed on a glass surface and then introduced at the focal point. The superhydrophobic
 94 surfaces consist of micro-scale cylindrical pillars of $5.5 \mu\text{m}$ in diameter (D) and $5 \mu\text{m}$ in
 95 height (H) organized in a square lattice. SHS 1 and 2 have a periodicity P of $14.1 \mu\text{m}$ and
 96 $7.6 \mu\text{m}$, respectively. Superhydrophobic surfaces were made by pouring liquid PDMS into
 97 a Si mold, vacuumed, cured, and finally peeled off as the samples. The PDMS surfaces
 98 were 3 mm thick. Once introduced at the focal point, surface dynamics is monitored by two
 99 high-speed cameras (Photron AX200 and AX100), while the HIFU transducer records the
 100 back scattering sound at low amplitude. A long range microscope is mounted on a camera to
 101 record from the side, while the second camera is used with a mirror to image the dynamic
 102 from the bottom (see Fig. 1).

103 3. Results and Discussion

104

3.1. Initial wetting state

105 The initial wetting state for the different surfaces is compared in Figure 2 using the bottom
 106 view and acoustic reflection at small amplitude. Glass, flat PDMS, and SH1 surfaces appear
 107 black from the bottom view, indicating that the light coming from the bottom is not reflected,
 108 and hence the solid surfaces are fully wet. The bottom view of the SH2 surface is much
 109 brighter, indicating that the bottom light is reflected by air-water interface, and thus an air
 110 layer is trapped inside the micro-structure. The stability of the Cassie-Baxter state has been
 111 predicted by Bico *et al.* (Bico *et al.* 2002) based on energy analysis. They show that an air

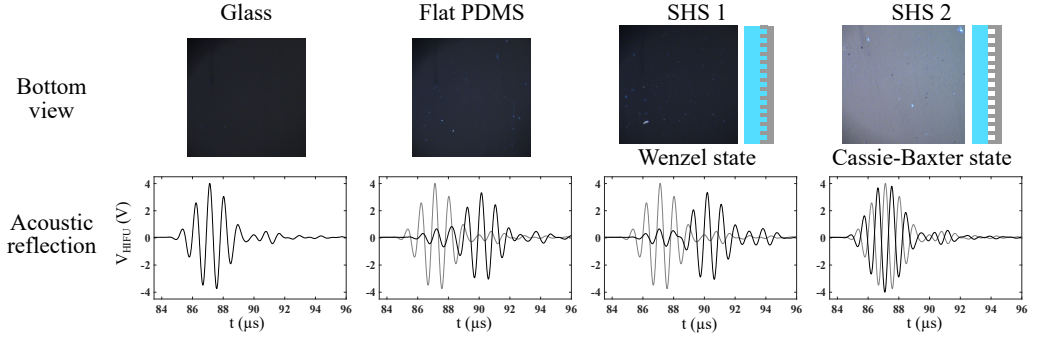


Figure 2: Comparison of the initial wetting state of the different solid surfaces submerged in water. The first row of images shows the bottom view by a high-speed camera, while the second row of data are the back-scattered sound detected by monitoring the voltage of the transducer. For comparison, the acoustic reflection from the glass surface solely (bottom left) is added in grey for the other surfaces.

112 layer will be stable if the contact angle of the constituting material on flat surface θ_f obeys:

$$113 \quad \theta_f > \theta_c, \text{ with } \cos \theta_c = \frac{\Phi - 1}{R - \Phi}, \quad (3.1)$$

114 where $R = 1 + \pi DH/P^2$ is the roughness, and $\Phi = (\pi D^2)/(4P^2)$ is the solid fraction. Our
 115 SH1 (SH2) has a roughness $R = 1.43$ ($R = 2.5$) and a solid fraction of $\Phi = 0.12$ ($\Phi = 0.41$),
 116 leading to a critical contact angle $\theta_c = 134^\circ$ ($\theta_c = 106^\circ$). The water contact angle on flat
 117 PDMS is $\theta_f = 110 - 115^\circ$ (Mata *et al.* 2005). In agreement with the theoretical prediction,
 118 the θ_f -value for the flat PDMS is smaller than θ_c for the SH1 surface so water invades the
 119 microstructure. For the SH2 surface $\theta_f > \theta_c$, therefore, a stable air layer is trapped between
 120 the micropillars, as observed in the experiments.

121 The back-scattered sound of the different surfaces is then analyzed at a small amplitude.
 122 The HIFU transducer voltage averaged over ten pulses is shown in Figure 2. For all surfaces,
 123 echoes are detected at $85 \mu s$, corresponding to the time required for an acoustic wave to travel
 124 to the focal point and return to the transducer. The reflected pulse has the same shape as the
 125 incoming pulse for the glass surface. For the flat PDMS and the SHS 1, the back-scattered
 126 pulse is more complex and consists of a first small amplitude reflection followed by a second
 127 higher reflection similar to the glass case. More surprisingly, the back-scattered sound from
 128 the SHS 2 is only made of a strong pulse with a π -phase change, compared to the incoming
 129 pulse.

130 These observations can be explained using linear acoustics. The pressure reflection
 131 coefficient (r) of acoustic plane waves on an interface is given by $r_{i,j} = (Z_j - Z_i)/(Z_i + Z_j)$,
 132 with $Z_i = \rho_i c_i$ the acoustic impedance, ρ_i and c_i the density and sound velocity in the
 133 media i . The subscript i (j) represents the media supporting the incident (transmitted) pulse.
 134 The different interfaces present in our experiments have the following reflection coefficient:
 135 $r_{w,g} = 0.8$ for water/glass interface, $r_{w,p} = -0.18$ for water/PDMS, $r_{w,a} = -1$ for water/air
 136 and $r_{p,g} = 0.85$ for PDMS/glass (Xu *et al.* 2020). For the water-glass interface, $r_{w,g}$ is
 137 positive and close to 1, and the back-scattered pulse is expected to be of high amplitude
 138 without phase change as observed in Figure 2. The flat PDMS and SH1 surfaces are held by
 139 a glass plate, and the incoming pulse will first encounter the water/PDMS interface leading
 140 to a first weak reflection since $r_{w,p}$ is small. A non-negligible part of the pulse is transmitted
 141 to the PDMS and then reflected by the PDMS/glass interface, generating the second strong
 142 echo since $r_{p,g}$ is high.

143 Finally, the back-scattered sound coming from the SH2 surface is solely made of a strong

144 pulse with π -phase change, in agreement with a reflection on a water/air interface as $r_{w,a} =$
 145 -1 . This confirms the presence of an air layer inside SH2 microstructure as optically observed,
 146 demonstrating that acoustics can be of great use to probe plastron stability. The absolute
 147 value of the reflection coefficient of the water/air interface is higher than the coefficient of
 148 water/glass ($|r_{w,a}| > |r_{w,g}|$). The amplitude of the back-scattered signal from SHS 2 should
 149 therefore be higher than the one from the glass surface, but the measured reflections are of
 150 similar amplitude (see Figure 2). This discrepancy might be ascribed to the fact that the SH2
 151 interface is not a pure water/air interface but a mixture of water/air and PDMS pillars (41%
 152 of the surface is PDMS), which modifies the reflection coefficient.

153

3.2. Cavitation behavior

154

155 The solid surfaces were subjected to high-intensity pulses of different amplitudes to
 156 characterize their cavitation behavior. The cavitation is monitored by side-view images
 157 [see Figure 3 (b)-(c)] taken during the acoustic excitation when cavitation clouds are visible.
 158 The area of such cavitation cloud (A_{cav}) is measured and compared for the different surfaces
 159 under various excitation amplitudes in Figure 3 (a). Although the data are scattered, which is
 160 expected for cavitation experiments, it can be seen that only a few small cavitation bubbles
 161 appear on flat PDMS and on the SHS 1. In contrast, significant cavitation is observed on
 162 the glass surface and the SHS 2. The flat glass surface exhibits cavitation at low acoustic
 162 excitation, while cavitation cloud appears later for SHS 2.

163

164 The ability of surfaces or liquids to cavitate under relatively small pressure excitation, well
 165 above the spinodal pressure of water (~ -140 MPa) (Zheng *et al.* 1991), is determined by
 166 the presence of micro/nanobubbles trapped in surface defects or impurities, called cavitation
 167 nuclei (Harvey *et al.* 1944). Stabilisation of such nuclei on a surface requires a hydrophobic
 168 geometrical defect called crevice (Atchley & Prosperetti 1989; Bussonniere *et al.* 2020).
 169 When subjected to low enough negative pressure (i.e., cavitation threshold), such nuclei
 169 become mechanically unstable, and cavitation bubbles appear.

170

171 The different cavitation responses are therefore either due to a difference in nuclei
 172 population and/or in local negative pressure. The first nuclei source in the experiments
 173 comes from tap water, which contains many impurities and thus a large number of nuclei.
 174 However, the same water was used in all experiments, and hence these nuclei could not
 175 explain the cavitation differences observed. The second source of nuclei comes from the
 176 different solid surfaces. PDMS is naturally hydrophobic, which should favor nuclei trapping
 177 compared to hydrophilic glass. However, this soft material is expected to have little, if no,
 178 sharp defect (crack-like) due to its polymerization from a liquid form, which can explain that
 179 almost no cavitation on flat PDMS was detected (Figure 3). Similarly, SHS 1 in a Wenzel
 180 wetting state, although being micro-textured with cylindrical pillars, is not expected to have
 181 sharp crevices, which can explain the small cavitation activity observed. Glass, on the other
 182 hand, can have small cracks potentially leading to significant cavitation activity as observed
 182 on glass.

183

184 The other important factor for cavitation is the local negative pressure, which is greatly
 185 influenced by the acoustic boundary condition. The acoustic wave reflected by a surface with
 186 a factor of r interferes with the incident wave resulting in a local minimum pressure, which
 187 can greatly differ from the incident minimum pressure, $P_{\text{min}}^{\text{inc}}$. For example, at the interface
 188 between water and a surface j , the minimum pressure is $P_j^{\text{wall}} = (1+r_{w,j}) P_{\text{min}}^{\text{inc}}$. The minimum
 189 pressure is therefore amplified on the glass surface ($P_{\text{glass}}^{\text{wall}} = 1.8 P_{\text{min}}^{\text{inc}}$), reduced on flat PDMS
 190 and SHS 1 ($P_{\text{pdms,shs1}}^{\text{wall}} = 0.8 P_{\text{min}}^{\text{inc}}$), or almost cancelled on SHS 2 ($P_{\text{shs2}}^{\text{wall}} \approx 0$). This simplified
 191 analysis is in agreement with the experiments where cavitation clouds appear on the surface
 191 for glass [Figure 3 (b)], whereas no cavitation is observed upon the surface of SHS 2 (Figure

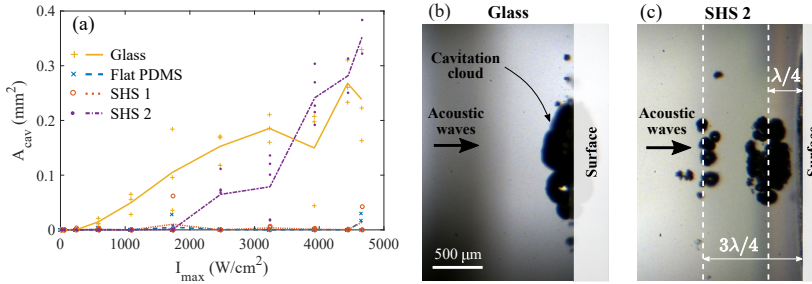


Figure 3: (a) Area of the cavitation cloud (A_{cav} , captured from the side-view) as a function of the maximum incident acoustic intensity (I_{max}) for the different solid surfaces. Points in (a) represent the area of one experiment, while the solid lines represent the average values. (b)-(c) Side-view images of the cavitation cloud on glass surface [in (b)] and on the superhydrophobic surface 2 [in (c)] appearing for an incident maximum intensity of 3.9 kW/cm^2 .

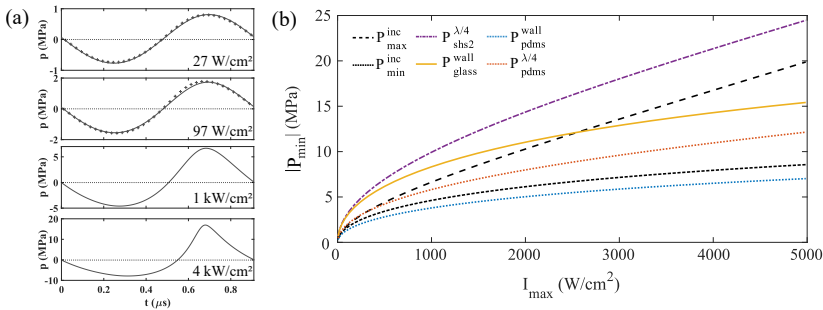


Figure 4: (a) Incident waveform at the focal plan for different maximum incident intensity (I_{max}). The simulation results (solid lines) using the nonlinear acoustic code (Soneson 2009) are compared to the experimental measurements (cross points) at low intensity. (b) Evolution of the minimum and maximum incident pressure ($P_{min, max}^{inc}$) and of the minimum local pressure ($P_{min}^{position, surface}$) at specific position for a surface with the maximum incident intensity (I_{max}).

192 3 (c)). Note that the small bubbles in Figure 3 (b) top are actually on the surface, although
 193 appearing away from it due to the slight tilt between the camera and the surface.

194 Interference between the incident and reflected waves also occurs away from the surface.
 195 If a continuous excitation was used, a standing wave in the liquid would have been generated.
 196 However, here, we use short pulses with only 2 periods with a significant amplitude. Wave
 197 interference therefore only occurs in the surface vicinity, in a region of approximately one
 198 wavelength (λ). Local minimums generated by the transient standing wave depend on the
 199 reflection coefficient sign. If $r > 0$, the pressure anti-nodes are located on the surface, at $\lambda/2$
 200 and λ away from the surface. Differently, if $r < 0$ the minimum pressures are located at $\lambda/4$
 201 and $3\lambda/4$ away from the surface. The above analysis may be consistent with the experimental
 202 data, which reveals that cavitation cloud appears at $\lambda/4$ and $3\lambda/4$ for the SHS2 experiments.
 203 However, with the analysis one would have expected appearance of cavitation at λ and $\lambda/2$
 204 in the experiments with the glass surface and not only on the surface.

205 To understand this discrepancy for the glass surface, one needs to analyze the high acoustic
 206 intensity used in the experiments. Under such strong excitation, the acoustic propagation is
 207 nonlinear, and the acoustic waveform departs from a simple cosine function, as shown in
 208 Figure 4 (a). The solid lines represent the results from the nonlinear acoustic simulations.
 209 The simulation results are in good agreement with the experimental data (crosses) at low
 210 values of I_{max} . Note that the measurements at the focal point can only be performed at low

211 intensity to prevent deterioration of the hydrophone by cavitation. As detailed in the appendix
 212 **A**, the acoustic field at high intensity was calibrated by measuring the pressure at the second
 213 pressure lobe (after the focal region). As I_{max} increases, the waveform become asymmetric,
 214 and the maximum incident pressure P_{max}^{inc} increases faster than the absolute minimum pressure
 215 $|P_{min}^{inc}|$, as shown in figure 4 (b).

216 Such asymmetry has important implications in the local minimum generated in the
 217 interference region. For $r > 0$, the local minimums located at $\lambda, \lambda/2$ and on the wall are equal
 218 to $P_j^\lambda = P_j^{\lambda/2} = P_j^{wall} = (1+r_{w,j}) P_{min}^{inc}$. However, for $r < 0$, the reflected wave is inverted (with
 219 a phase change by π), and the local minimum pressures are $P_j^{3\lambda/4} = P_j^{\lambda/4} = P_{min}^{inc} - r_{w,j} P_{max}^{inc}$.
 220 Figure 4 (b) shows the minimum pressures generated by the combination of nonlinear
 221 acoustic and the reflection for the different surfaces. As the reflection from SHS2 at low
 222 intensity (Figure 2) has the same amplitude as the glass surface, we use $r_{w,shs2} = -0.8$
 223 to better estimate the reflection. Due to the reflection of the strong maximum incident
 224 pressure, minimum pressures in SHS2 experiments reach the lowest level, which explains
 225 the biggest cavitation cloud observed. Cavitation with SHS2 appears at $I = 2.5 \text{ kW/cm}^2$,
 226 i.e., at $P_{shs2}^{\lambda/4} \approx -16 \text{ MPa}$, which corresponds to the threshold for cloud cavitation in water.
 227 Pressure in the glass experiment only reaches $P_{glass}^{wall} \approx -15 \text{ MPa}$ at the maximum intensity.
 228 This explains why no clouds are observed in water for the glass cases. Cavitation, in this case,
 229 occurs only on the glass interface due to the presence of surface nuclei. It should be noted
 230 that the nonlinear waveform reflected with a phase shift by π is unstable and will recover to
 231 a sine wave at the transducer, shown by Tanter *et al.* (2001).

232

3.3. Wetting transition

233 The stability of the superhydrophobic state is also studied by using the bottom camera and the
 234 acoustic reflection at a small amplitude. Figure 5 (a) shows the images from the bottom taken
 235 after the exposition of the SHS 2 to different intense acoustic pulses. Note that the surface is
 236 moved between each high impulsion experiment, so each trial is performed on a fresh area
 237 of the SHS. For intensities smaller than $\approx 0.1 \text{ kW/cm}^2$, the air layer remains unchanged, as
 238 shown by the brownish color. Starting at 0.25 kW/cm^2 , a change in color is observed, and
 239 clear interference color pattern appears at 0.59 W/cm^2 . These colors arise from the white
 240 light interference inside the air layer of the SHS and indicate that the air-layer thickness has
 241 been decreased at the focal region due to the acoustic pulse. For $I_{max} > 1.1 \text{ kW/cm}^2$, a
 242 dark disk appears in the center surrounded by interference fringes. The radius of this disk
 243 increases with the acoustic intensity, and its evolution with I_{max} is reported in Figure 5 (c).

244 This black disk might correspond to a local superhydrophobic breakdown (i.e., wetting
 245 transition) since SHS 1, which didn't trapped an air layer, appears black in Figure 2. To
 246 verify this, the acoustic reflection signals at low amplitude from the SHS 2 surface before
 247 (shown in dashed blue) and after (shown in red) an intense acoustic pulse of 2.5 kW/cm^2
 248 are compared in Figure 5 (b). Before, the reflection corresponds to an air-water reflection
 249 as shown in Figure 2. The reflection after the high intensity pulse is drastically changed
 250 and is similar to the reflection of SHS 1 of Figure 2. This observation confirms that high
 251 intensity pulses trigger a local wetting transition, corresponding to the dark area where water
 252 penetrates inside the microstructure. It should be note that this transition occurs at amplitude
 253 smaller ($I_{max} = 1.1 \text{ kW/cm}^2$) than the appearance of cavitation cloud ($I_{max} = 2.5 \text{ kW/cm}^2$),
 254 ruling out a transition driven by cavitation.

255 The transition from a Cassie-Baxter to a Wenzel wetting state is usually understood by
 256 looking at the local force balance of the air-water interface in contact with the microstructure.
 257 A small pressure increase in the liquid phase is balanced by a capillary pressure arising from

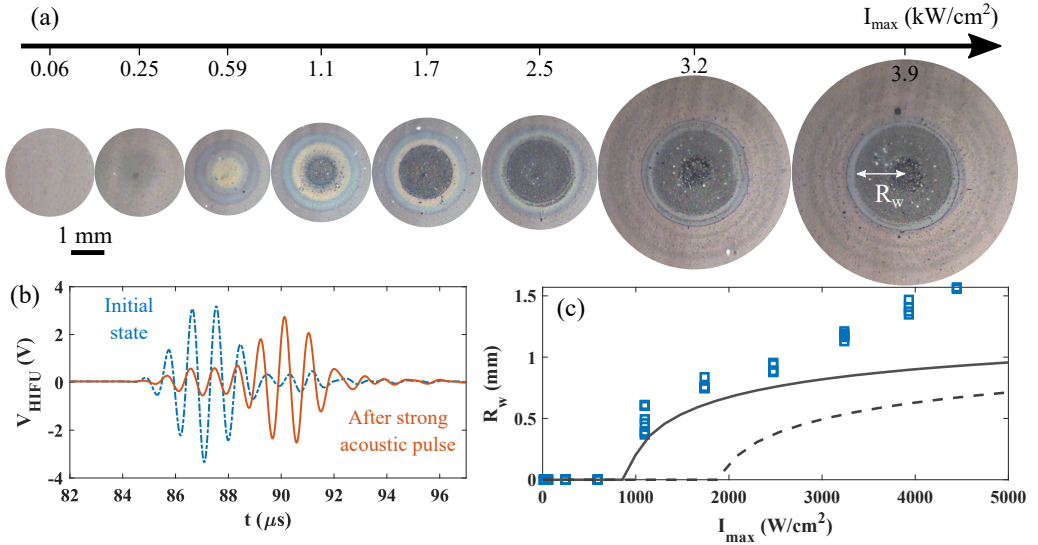


Figure 5: (a) Bottom view of the SHS 2 after exposition of different high intensity acoustic pulses showing the apparition of interference fringes and a wetted region in black of radius (R_w). (b) Acoustic reflection of the SHS 2 of a small amplitude pulse before (blue) and after (red) the exposition of a high intensity pulse of $I_{\max} = 2.5 \text{ kW/cm}^2$. (c) Evolution of the wetted radius (R_w) observed experimentally as a function of the maximum acoustic intensity (I_{\max}). The solid and dashed lines correspond the wetted radius predicted by the sliding and touch-down models, respectively.

258 the bending of the interface between pillars (Quéré 2008). At higher liquid pressure, the
 259 interface can either touch the bottom of the SHS (i.e., touch-down scenario) or slide on the
 260 pillar when the local contact angle on pillars reaches the advancing one (i.e., sliding scenario)
 261 (Moulinet & Bartolo 2007; Reyssat *et al.* 2007). These different scenarios are associated with
 262 two critical liquid pressures:

$$263 \quad p_t^c \approx \frac{2\gamma H}{(\sqrt{2}P - D)^2}, \quad (3.2)$$

264 for the touch-down, with γ the air-water surface tension, and θ_a the advancing contact angle;
 265 for the sliding (Moulinet & Bartolo 2007):

$$266 \quad p_s^c = \frac{2\Phi}{1 - \Phi} |\cos \theta_a| \frac{2\gamma}{D}. \quad (3.3)$$

267 Previously, we showed that the oscillating acoustic pressure at the SHS 2 interface almost
 268 vanishes due to the acoustic boundary condition, and thus the high oscillating acoustic
 269 pressure (at 1.1 MHz) cannot explain the wetting transition. Nonetheless, acoustic waves
 270 are known to apply radiation pressure on interfaces (Borgnis 1952) and are commonly used
 271 to trap objects in acoustofluidics (Bruus 2012). Such radiation forces arise from a change
 272 of media momentum induced by the acoustic scattering or reflection of an interface or an
 273 object (Westervelt 1957; Baresch *et al.* 2013). These radiation forces originate from the
 274 difference of the time-averaged acoustic energy density, i.e., radiation pressure, across the
 275 interface. It is a cumulative process, and these forces hence occur on a longer timescale than
 276 the fast-oscillating acoustic pressure. If we assume that the SHS 2 behaves as a pure water-air
 277 interface and an incident angle of 90° , the radiation pressure applied on the interface is given

278 by (Borgnis 1952):

$$279 \quad p_{\text{rad}}(r) = \frac{2I(r)}{c}, \quad (3.4)$$

280 with I the incident acoustic intensity, c sound speed in water, and r the radial coordinate on
 281 the surface centered on the focal axis. The acoustic intensity, and thus the radiation pressure,
 282 depends on r due to the HIFU geometry as shown in Figure 6 (b). The wetting transition
 283 would occur if $p_{\text{rad}} > p_{s,t}^c$, and a critical radius r_c can be extracted from the simulated
 284 intensity field whereby $p_{\text{rad}}(r_c) = p_{s,t}^c$. The predictions for r_c using the sliding and touch-
 285 down models presented above are compared with the experimental data in Figure 5 (c) for
 286 $\theta_a = 110^\circ$.

287 This simplified model predicts the beginning of the transition around $I_{\text{max}} = 900 \text{ W/cm}^2$
 288 for the sliding scenario, which is in good agreement with the experimental data. Moreover,
 289 the wetted radius R_w agrees well with the critical radius predicted in the range 1 – 2.5
 290 kW/cm^2 of I_{max} . The good agreement indicates that the wetting transition occurs where the
 291 acoustic beam is more intense and also validates the wetting transition driven by radiation
 292 pressure. It should be noted that the interference pattern starts to appear at a lower intensity
 293 (see Figure 5 (a) for $I_{\text{max}} = 0.59 \text{ kW/cm}^2$). This may suggest that the interface starts to slide
 294 at lower radiation pressure than predicted but does not reach the microstructure bottom. A
 295 more comprehensive analysis involving time dependence, similar to the one done for free
 296 surface in (Issenmann *et al.* 2011), is needed to better understand the interface motion under
 297 radiation pressure. In addition to developing such a complex model, a study of the influence
 298 of pulse duration and a better acoustic calibration would be needed to fully capture the
 299 interface dynamic in the future.

300 For larger intensity, the water penetration area is underestimated by the sliding model.
 301 This deviation coincides with the appearance of an intense cavitation cloud, which can reflect
 302 acoustic wave and also create strong pressure during its collapse. Therefore, the local acoustic
 303 field is expected to greatly differ from the simple combination of an incident and reflected
 304 wave, thereby modifying the radiation pressure on the surface. Note that the local acoustic
 305 field can be inferred from the imprint left on the SH surface. In Figure 5 (a), concentric grey
 306 circles surrounding the wetted area appear and are spaced by $\approx \lambda/4$. However, such circles
 307 cannot be explained by the secondary lobes of the incident beam, spaced by $\approx \lambda$ (see Figure
 308 6 (b)), which tends to support a strong modification of the acoustic field by the cavitation
 309 cloud.

310 4. Conclusions

311 We investigate the acoustic responses of superhydrophobic surfaces subjected to short intense
 312 pulses. Experiments at low amplitude reveal that when a SHS is able to stabilize an air layer
 313 (in a Cassie-Baxter state) the acoustic waves are reflected with a π phase-shift similar to an
 314 air-water interface. In a Wenzel state, a patterned surface behaves as a flat surface of the
 315 same material, and the microstructure has no influence on the acoustic reflection.

316 At high amplitude, intense cavitation is observed for the glass surface and SHS in (Cassie-
 317 Baxter) gas-trapping state, while almost no cavitation is detected for flat PDMS surface and
 318 PDMS SHS in a Wenzel state. This difference is mainly attributed to the acoustic boundary
 319 condition. For hard material, such as glass, the pressure on the solid surface is nearly doubled,
 320 leading to the appearance of a cavitation cloud on the surface. For the flat and wetted patterned
 321 PDMS surfaces (i.e., flat and SHS in Wenzel), the pressure on the surface is slightly lowered
 322 due to the close match in acoustic impedance with water. For SHS in a Cassie-Baxter state,
 323 the interference between the reflected and the incident wave results in a significant negative

324 pressure away from the surface (at $\lambda/4$ and $3\lambda/4$), where intense cavitation clouds form.
 325 Moreover, cavitation, in this case, is amplified by the conversion of the strong high pressure
 326 peaks arising from nonlinear propagation into great negative pressure by the reflection on
 327 the air layer.

328 The Wetting transition from Cassie to Wenzel state is observed at moderate intensity
 329 before cavitation appearance. The transition is shown to be driven by the acoustic radiation
 330 pressure, which overcomes the critical capillary pressure required to let the interface slide
 331 into the microstructure. The simplified model proposed well captures the transition and the
 332 size of Wenzel area at moderate intensities. For higher intensity, strong interaction with the
 333 cavitation cloud is expected to modify the local acoustic field, resulting in a deviation with
 334 the proposed model.

335 Underwater superhydrophobic surfaces are mainly studied in the context of drag reduction.
 336 In such an application, pressure on the plastron is governed by the hydrodynamic, and the flow
 337 can trigger a wetting transition. In this context, our results at low amplitude can contribute to
 338 developing non-destructive acoustic monitoring of the plastron stability. Moreover, the critical
 339 breakdown pressure of a superhydrophobic coating could be characterized and measured
 340 using acoustic pulses at moderate intensity. For future studies, an accurate measurement of
 341 this breakdown pressure would require a better calibration of the acoustic field and more
 342 extensive studies on the influence of the pulse duration and excitation frequency.

343

344 **Acknowledgements.** A.B. thanks Professor R. Wunenburger for fruitful discussions.

345

346 **Funding.** This work was supported by the Collaborative Research and Development (CRD) of the
 347 Natural Sciences and Engineering Research Council of Canada (NSERC) and the Canadian Centre for
 348 Clean Coal/Carbon and Mineral Processing Technologies (C5MPT). P.A.T. holds a Canada Research Chair
 349 (CRC) in Fluids and Interfaces. This research was undertaken, in part, thanks to funding from the CRC
 350 Program.

351

352 **Declaration of interest.** The authors report no conflict of interest.

353 Appendix A. Acoustic calibration

354 The acoustic field is first mapped at low amplitude using a needle hydrophone mounted on a 3-axis stage.
 355 This field is then used to find the parameter of the HIFU transducer (focal length and radius) in the nonlinear
 356 simulation (Soneson 2009). The axial distribution, z , the distance from the transducer, is measured along
 357 the axisymmetric axis and shown in Figure 6 (a). The simulated field captures well the pressure field in the
 358 focal region and peripheral lobes. Nonetheless, a slight deviation is observed for z below 40 mm. The radial
 359 distribution shown in Figure 6 (b) is measured in a plane perpendicular to the z -axis at the maximum pressure,
 360 i.e., at $z = 62$ mm. The simulation results are in good agreement with the experimental measurements.

361 At higher amplitude, cavitation occurs in the focal region, and no direct measurement can be performed
 362 using the hydrophone (as the intense cavitation can damage the hydrophone). Therefore, the nonlinear
 363 simulation is used to obtain the pressure at high intensity. The unknown in the simulation is the pressure
 364 impose at the transducer surface (p_{sim}). In the experiment, we impose a voltage at the output of the generator
 365 (V_{gen}) which is then amplify and converted into pressure by the HIFU. To calibrate our experiment using the
 366 simulation we therefore need to find the relation between p_{sim} and V_{gen} . To find such relation we measured the
 367 maximum and minimum pressure ($p_{\text{max}}^{\text{foc}}$ and $p_{\text{min}}^{\text{foc}}$) at low amplitude at $z = 62$ mm (in the focal region) and
 368 over a large range of voltage in the secondary lobes ($p_{\text{max}}^{2\text{nd}}$ and $p_{\text{min}}^{2\text{nd}}$) located at $z = 81$ mm. Simulations were
 369 then performed for different amplitudes of p_{sim} , and the functions $p_{\text{max}}^{\text{foc}}(p_{\text{sim}})$, $p_{\text{min}}^{\text{foc}}(p_{\text{sim}})$, $p_{\text{max}}^{2\text{nd}}(p_{\text{sim}})$ and
 370 $p_{\text{min}}^{2\text{nd}}(p_{\text{sim}})$ were extracted. These functions were inverted to convert the experimental measurement into
 371 p_{sim} values. In Figure 6 (c), we show the results of this treatment as a function of V_{gen} . All the experimental
 372 points collapse into a single line, which is fitted with a 3rd-order polynomial without a constant term. Note
 373 that the curve tends to saturate, which seems to indicate a saturation of the voltage amplifier limited to 200
 374 W (E&I 1020L).

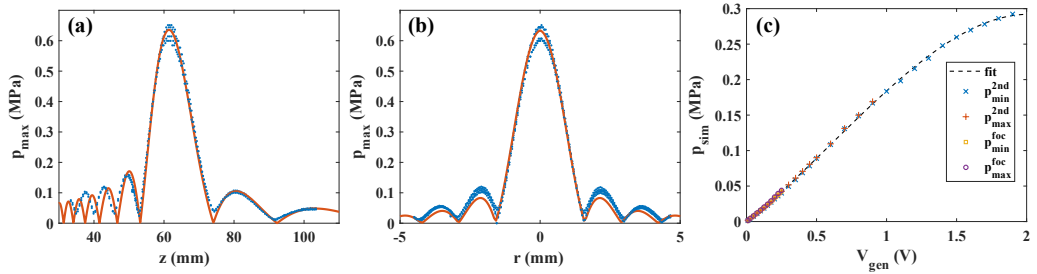


Figure 6: Evolution of the maximum acoustic pressure in the axial (a) and radial (b) direction at low amplitude. The red lines correspond to the prediction of the acoustic simulation using the non-linear code (Soneson 2009), while the blue dots represent the experimental points. (c) Evolution of the input pressure of the simulation (p_{sim}) fitting the different maximum and minimum measurements as a function of the generator voltage (V_{gen}).

REFERENCES

- 375 ALDHALEAI, AHMED & TSAI, PEICHUN AMY 2022 Evaporation dynamics of surfactant-laden droplets on a
376 superhydrophobic surface: Influence of surfactant concentration. *Langmuir* **38** (1), 593–601.
- 377 ATCHLEY, A. A. & PROSPERETTI, A. 1989 The crevice model of bubble nucleation. *The Journal of the*
378 *Acoustical Society of America* **86** (3), 1065–1084.
- 379 BARESCHE, DIEGO, THOMAS, JEAN-LOUIS & MARCHIANO, RÉGIS 2013 Three-dimensional acoustic radiation
380 force on an arbitrarily located elastic sphere. *The Journal of the Acoustical Society of America* **133** (1),
381 25–36.
- 382 BARTOLO, DENIS, BOUAMRIRENE, FARID, VERNEUIL, EMILIE, BUGUIN, AXEL, SILBERZAN, PASCAL &
383 MOULINET, SÉBASTIEN 2006 Bouncing or sticky droplets: Impalement transitions on superhydrophobic
384 micropatterned surfaces. *EPL (Europhysics Letters)* **74** (2), 299.
- 385 BICO, JOSÉ, THIELE, UWE & QUÉRÉ, DAVID 2002 Wetting of textured surfaces. *Colloids and Surfaces A:*
386 *Physicochemical and Engineering Aspects* **206** (1-3), 41–46.
- 387 BOBBI, MUSUVATHI S, KUMAR, S VIJAY, ASTHANA, ASHISH & GOVARDHAN, RAGHURAMAN N 2009
388 Underwater sustainability of the “cassie” state of wetting. *Langmuir* **25** (20), 12120–12126.
- 389 BORGNIS, FE 1952 Acoustic radiation pressure of plane-compressional waves at oblique incidence. *The*
390 *Journal of the Acoustical Society of America* **24** (5), 468–469.
- 391 BORMASHENKO, EDWARD, POGREB, ROMAN, WHYMAN, GENE & ERLICH, MORDEHAI 2007 Cassie- wenzel
392 wetting transition in vibrating drops deposited on rough surfaces: Is the dynamic cassie- wenzel
393 wetting transition a 2d or 1d affair? *Langmuir* **23** (12), 6501–6503.
- 394 BRUUS, HENRIK 2012 Acoustofluidics 7: The acoustic radiation force on small particles. *Lab on a Chip*
395 **12** (6), 1014–1021.
- 396 BUSSONNIÈRE, ADRIEN, BIGDELI, MASOUD B, CHUEH, DI-YEN, LIU, QINGXIA, CHEN, PEILIN & TSAI,
397 PEICHUN AMY 2017 Universal wetting transition of an evaporating water droplet on hydrophobic
398 micro- and nano-structures. *Soft matter* **13** (5), 978–984.
- 399 BUSSONNIÈRE, ADRIEN, LIU, QINGXIA & TSAI, PEICHUN AMY 2020 Cavitation nuclei regeneration in a
400 water-particle suspension. *Physical Review Letters* **124** (3), 034501.
- 401 CASTAGNA, MARCO, MAZELLIER, NICOLAS & KOURTA, AZEDDINE 2018 Wake of super-hydrophobic falling
402 spheres: influence of the air layer deformation. *Journal of Fluid Mechanics* **850**, 646–673.
- 403 DUFOUR, RENAUD, SAAD, NADINE, CARLIER, JULIEN, CAMPISTRON, PIERRE, NASSAR, GEORGE, TOUBAL,
404 MALIKA, BOUKHERROUB, RABAH, SENEZ, VINCENT, NONGAILLARD, BERTRAND & THOMY, VINCENT
405 2013 Acoustic tracking of cassie to wenzel wetting transitions. *Langmuir* **29** (43), 13129–13134.
- 406 FENG, GUANG, LI, FENGPING, XUE, WEI, SUN, KE, YANG, HUAN, PAN, QIAOFEI & CAO, YU 2019 Laser
407 textured grfp superhydrophobic surface as an underwater acoustic absorption metasurface. *Applied*
408 *Surface Science* **463**, 741–746.
- 409 HARVEY, E. N., BARNES, D. K., McELROY, W. D., WHITELEY, A. H., PEASE, D. C. & COOPER, K. W. 1944
410 Bubble formation in animals. i. physical factors. *Journal of Cellular and Comparative Physiology*
411 **24** (1), 1–22.
- 412 ISSENMANN, BRUNO, WUNENBURGER, RÉGIS, CHRAIBI, HAMZA, GANDIL, MORGANE & DELVILLE, J-P 2011

- 413 Unsteady deformations of a free liquid surface caused by radiation pressure. *Journal of fluid mechanics*
 414 **682**, 460–490.
- 415 JUNG, YONG CHAE & BHUSHAN, BHARAT 2007 Wetting transition of water droplets on superhydrophobic
 416 patterned surfaces. *Scripta Materialia* **57** (12), 1057–1060.
- 417 KARATAY, ELIF, HAASE, A. SANDER, VISSER, CLAAS WILLEM, SUN, CHAO, LOHSE, DETLEF, TSAI,
 418 PEICHUN AMY & LAMMERTINK, ROB G. H. 2013 Control of slippage with tunable bubble mattresses.
 419 *PNAS* **110** (21), 8422–8426.
- 420 LAFUMA, AURÉLIE & QUÉRÉ, DAVID 2003 Superhydrophobic states. *Nature materials* **2** (7), 457–460.
- 421 LI, SIZHE, LAMANT, SEBASTIEN, CARLIER, JULIEN, TOUBAL, MALIKA, CAMPISTRON, PIERRE, XU, XIUMEI,
 422 VEREECKE, GUY, SENEZ, VINCENT, THOMY, VINCENT & NONGAILLARD, BERTRAND 2014 High-
 423 frequency acoustic for nanostructure wetting characterization. *Langmuir* **30** (25), 7601–7608.
- 424 LV, PENGYU, XUE, YAHUI, SHI, YIPENG, LIN, HAO & DUAN, HUILING 2014 Metastable states and wetting
 425 transition of submerged superhydrophobic structures. *Physical review letters* **112** (19), 196101.
- 426 MARUVADA, S., LIU, Y., SONESON, J. E., HERMAN, B. A. & HARRIS, G. R. 2015 Comparison between
 427 experimental and computational methods for the acoustic and thermal characterization of therapeutic
 428 ultrasound fields. *J. Acoust. Soc. Am.* **137** (4), 1704–1713.
- 429 MATA, A., FLEISCHMAN, A. J. & ROY, S. 2005 Characterization of polydimethylsiloxane (pdms) properties
 430 for biomedical micro/nanosystems. *Biomed. Microdevices* **7** (4), 281–293.
- 431 MCHALE, GLEN, AQIL, SANAA, SHIRTCLIFFE, NJ, NEWTON, MI & ERBIL, H YILDIRIM 2005 Analysis of
 432 droplet evaporation on a superhydrophobic surface. *Langmuir* **21** (24), 11053–11060.
- 433 MOULINET, S & BARTOLO, D 2007 Life and death of a fakir droplet: Impalement transitions on
 434 superhydrophobic surfaces. *The European Physical Journal E* **24** (3), 251–260.
- 435 PAPADOPOULOS, PERIKLIS, MAMMEN, LENA, DENG, XU, VOLLMER, DORIS & BUTT, HANS-JÜRGEN 2013
 436 How superhydrophobicity breaks down. *Proceedings of the National Academy of Sciences* **110** (9),
 437 3254–3258.
- 438 POETES, ROSA, HOLTZMANN, KATHRIN, FRANZE, KRISTIAN & STEINER, ULLRICH 2010 Metastable underwater
 439 superhydrophobicity. *Physical review letters* **105** (16), 166104.
- 440 QUÉRÉ, DAVID 2008 Wetting and roughness. *Annual review of materials research* **38** (1), 71–99.
- 441 REYSSAT, MATHILDE, YEOMANS, JULIA M & QUÉRÉ, DAVID 2007 Impalement of fakir drops. *EPL*
 442 (*Europhysics Letters*) **81** (2), 26006.
- 443 ROTHSTEIN, JONATHAN P 2010 Slip on superhydrophobic surfaces. *Annual review of fluid mechanics* **42**,
 444 89–109.
- 445 SAAD, N, DUFOUR, R, CAMPISTRON, PIERRE, NASSAR, GEORGES, CARLIER, JULIEN, HARNOIS, M, MERHEB,
 446 B, BOUKHERROUB, R, SENEZ, V, GAO, J & OTHERS 2012 Characterization of the state of a droplet on a
 447 micro-textured silicon wafer using ultrasound. *Journal of Applied Physics* **112** (10), 104908.
- 448 SEO, JONGMIN, GARCÍA-MAYORAL, RICARDO & MANI, ALI 2018 Turbulent flows over superhydrophobic
 449 surfaces: flow-induced capillary waves, and robustness of air–water interfaces. *Journal of Fluid*
 450 *Mechanics* **835**, 45–85.
- 451 SHARDT, NADIA, BIGDELI, MASOUD BOZORG, ELLIOTT, JANET A. W. & TSAI, PEICHUN AMY 2019 How
 452 surfactants affect droplet wetting on hydrophobic microstructures. *J. Phys. Chem. Letts.* **10** (23),
 453 7510–7515.
- 454 SONESON, J. E 2009 A user-friendly software package for hifu simulation. In *AIP Conference Proceedings*,
 455 , vol. 1113, pp. 165–169. American Institute of Physics.
- 456 SUDEEPTHI, AREMANDA, YEO, LESLIE & SEN, AK 2020 Cassie–wenzel wetting transition on nanostructured
 457 superhydrophobic surfaces induced by surface acoustic waves. *Applied Physics Letters* **116** (9),
 458 093704.
- 459 TANTER, MICKAËL, THOMAS, JEAN-LOUIS, COULOUVRAT, FRANÇOIS & FINK, MATHIAS 2001 Breaking of
 460 time reversal invariance in nonlinear acoustics. *Physical review E* **64** (1), 016602.
- 461 TONG, LEI, XIONG, ZHU, SHEN, YA-XI, PENG, YU-GUI, HUANG, XIN-YU, YE, LEI, TANG, MING, CAI, FEI-
 462 YAN, ZHENG, HAI-RONG, XU, JIAN-BIN & OTHERS 2020 An acoustic meta-skin insulator. *Advanced*
 463 *Materials* **32** (37), 2002251.
- 464 TSAI, PEICHUN, LAMMERTINK, ROB G. H., WESSLING, MATTHIAS & LOHSE, DETLEF 2010 Evaporation-
 465 triggered wetting transition for water droplets upon hydrophobic microstructures. *Phys. Rev. Lett.*
 466 **104**, 116102.
- 467 VERHO, TUUKKA, KORHONEN, JUUSO T, SAINIEMI, LAURI, JOKINEN, VILLE, BOWER, CHRIS, FRANZE,
 468 KRISTIAN, FRANSILA, SAMI, ANDREW, PIERS, IKKALA, OLLI & RAS, ROBIN HA 2012 Reversible

- 469 switching between superhydrophobic states on a hierarchically structured surface. *Proceedings of the*
470 *National Academy of Sciences* **109** (26), 10210–10213.
- 471 WESTERVELT, PETER J 1957 Acoustic radiation pressure. *The Journal of the Acoustical Society of America*
472 **29** (1), 26–29.
- 473 XIANG, YAOLEI, HUANG, SHENGLIN, LV, PENGYU, XUE, YAHUI, SU, QIANG & DUAN, HUILING 2017 Ultimate
474 stable underwater superhydrophobic state. *Physical review letters* **119** (13), 134501.
- 475 XU, GUANGYAO, NI, ZHENGYANG, CHEN, XIZHOU, TU, JUAN, GUO, XIASHENG, BRUUS, HENRIK & ZHANG,
476 DONG 2020 Acoustic characterization of polydimethylsiloxane for microscale acoustofluidics. *Physical*
477 *Review Applied* **13** (5), 054069.
- 478 YOSHIMITSU, ZEN, NAKAJIMA, AKIRA, WATANABE, TOSHIYA & HASHIMOTO, KAZUHITO 2002 Effects of
479 surface structure on the hydrophobicity and sliding behavior of water droplets. *Langmuir* **18** (15),
480 5818–5822.
- 481 ZHENG, Q., DURBEN, D. J., WOLF, G. H. & ANGELL, C. A. 1991 Liquids at large negative pressures: water
482 at the homogeneous nucleation limit. *Science* **254** (5033), 829–832.